Infall as a Function of Position and Molecular Tracer in Dense Cores: Senior Honors Thesis

Jared Keown

Department of Physics and Astronomy, University of Louisville, 102 Natural Science Building, Louisville, KY 40292

jakeow01@louisville.edu

Abstract

The standard model of prestellar core collapse suggests that this process works from the inside and moves outwards, with the fastest motions at the center. The relative abundances of many molecules also vary within cores, with certain molecules found only in specific regions characterized by narrow ranges of temperature and density. These characteristics lead to the hypothesis that the observed infall speeds in starless cores depend on both the position of the observations and the molecular tracer chosen. By measuring line emission at multiple positions across a core using an array of tracer molecules, one can determine whether these theoretical dependencies match observational evidence. Although surveys of infall motions in dense cores have been carried out for years, very few surveys have been awarded enough time to map infall across cores using multiple spectral line observations. To fill this gap, we present IRAM 30m maps of N_2H^+(1-0), DCO^+(2-1), DCO^+(3-2) and HCO^+(3-2) emission towards two prestellar cores (L1544 and L694) and one protostellar core (L1521F). We find that the measured infall velocity varies as a function of position across each core and varies with the choice of molecular line, likely as a result of radial variations in core chemistry and dynamics.

1. Introduction

1.1. Core Physical Properties

Molecular gas and dust cores with densities of 10^5 cm^{-3}, temperatures around 10K and diameters approximately 0.1pc serve as the cocoons out of which stars are born (Di Francesco et al. 2007). An evolutionary stage classification scheme for these cores has been

developed in recent years based upon the presence, or lack thereof, a forming protostar. Those with observable submillimeter continuum emission, but lacking a detectable IRAS or infrared source, are generally characterized as "prestellar" because they have not yet formed a protostar (Ward-Thompson et al. 1994). These prestellar cores undergo collapse when the inward force of gravity overcomes the outward push of the internal pressure of the system. (Note that the use of "core collapse" throughout this paper refers to this initial star formation process rather than the collapse that occurs during the final stages of high-mass stellar evolution.) When collapse finally begins, the core is generally classified as "contracting" and it is said to be undergoing "infall" as its gas is moving inward toward its center. Conversely, when a core is expanding and material is being launched away from its center, an "outflow" is said to be present. Outflows are commonly found in "protostellar" cores, which are given their name due to the fact that they contain a detectable forming protostar or Very Low Luminosity Object (VeLLO) (Kauffmann et al. 2005). The newly formed star at the center of protostellar cores creates a disruption in the normal collapsing velocity pattern of the gas by fueling bipolar outflow jets. Simulations and visualization software have been developed by Bate et al. (2014), Price et al. (2012), and Price & Bate (2009) that provide a visual representation of the early stages of the star formation process. The group has created short videos that allow viewers to witness the contraction of molecular gas clouds to form dense cores, their subsequent collapse, and the turbulent outflows that are produced after a protostar has been formed. Still frames from a selection of these simulations are provided in Figures 1 and 2. Figure 1 outlines the processes involved during the collapse of a large molecular gas and dust cloud to form dense cores, while Figure 2 displays the evolution of the collimated outflow jets that are launched after the formation of a protostar.

Observations have found that infall is spatially extended across the highest column density regions of the core (Tafalla et al. 1998; Lee et al. 2001). Theoretical models predict

that collapse begins from the inside and moves out, with the fastest motions at the center (Shu 1977). However, there has not been sufficient observational data to confirm the theoretical prediction that the *speed* at which a core is contracting varies with distance from the center.

1.2. Core Chemical Properties

On the chemical level, position within the core plays a major factor in the relative abundances of many molecules in the gas phase. Certain carbon-based molecules, such as CO, freeze-out onto the surface of dust grains at temperatures around 10K and densities above 10^4 cm^{-3} (Caselli et al. 1999). As a result, gas phase CO, along with other carbon-bearing molecules, is significantly depleted toward core centers (Tafalla et al. 2002).

A side effect of CO depletion is the confinement of certain molecules to the centers of cores. Nitrogen-bearing molecules can survive in the gas phase at higher densities and lower temperatures than carbon-based molecules. This abundance differential was originally thought to stem from N_2, the mother particle of N-bearing molecules, having a lower binding energy to dust grains than CO, the mother particle of C-bearing molecules (Aikawa et al. 2001). However, laboratory studies by Bisschop et al. (2006) have invalidated this notion by showing that N_2 and CO have similar binding energies. Other theories link the disparity to the nitrogen atom, which does have a lower binding energy than CO, and suggest that it bonds to produce gas phase N_2 that can subsequently form larger N-bearing gas molecules (Di Francesco et al. 2007). One such molecule is N_2H^+, which is found only in the cold, high density inner regions of cores where its main reactants, e.g. CO and electrons, are depleted due to freeze-out (Di Francesco et al. 2007, see Figure 3 for a schematic representation). For a similar reason, deuterated molecules are also found only in core centers. CO prohibits the production of deuterium enriched particles in outer regions, but since it is depleted towards

the center, deuterated molecules with easily detectable rotational lines, such as N_2D^+, can be formed (Crapsi et al. 2005). Studies have also linked deuterium enrichment to chemical evolution, with a higher fraction of deuterated molecules corresponding to a more evolved core (Crapsi et al. 2005). Additionally, Schnee et al. (2013) found that cores with deuterium fractionation above 0.1 were more likely to have signatures of inward motions than cores with smaller deuterium ratios, further linking chemical evolution to dynamical evolution.

Based on our current understanding of the dynamics and chemistry of cores, it leads one to the conclusion that infall velocity may be dependent upon position inside the core. Infall speeds are theorized to decrease with distance from the core center under our current model of star formation; which implies a spatial dependency. Chemically, we also know that molecular abundances vary with position inside a core. Therefore, one would predict that the infall velocity measured from the spectra of different molecules should show variations as well.

1.3. Asymmetric Line Profiles

The emission from molecular rotational lines is used when observing the structure, kinematics and chemistry of dense cores (Bergin & Tafalla 2007). Based upon the shape of the observed emission line profile, one can determine various core properties, one of which is the infall/outflow velocity of the gas. Doppler shifts actually induce asymmetries in these spectra when observing either collapsing or expanding cores. When viewing a static core that is neither collapsing nor expanding, one sees a normal Gaussian distribution for a given emission line since equal amounts of the emission are moving toward (blueshifted) and away (redshifted) from the observer (see Figure 4). For a collapsing core (infall), the layer nearest to the observer's point of view is now redshifted since it is moving inward toward the core center. As molecular emission photons from the core pass through this

layer, some get reabsorbed by the redshifted molecules falling into the center which causes a dip in the redshifted end of the would-be Gaussian emission distribution. This process ultimately causes the observer to view an asymmetrically blue, double peaked spectrum with a blue peak brighter than a red peak (Lee & Myers 2011). For an expanding core (outflow), the layer nearest to the observer's point of view becomes blueshifted as material is being expelled from the innards of the core. The emission once again gets reabsorbed, only now it is in the blueshifted side of the distribution causing a diminished blue peak. Finally, the observer is left with a spectrum that is asymmetrically red with a red peak brighter than a blue peak.

Despite an abundance of surveys investigating infall motions (Lee et al. 1999, 2004; Sohn et al. 2007; Schnee et al. 2013, etc.), few have been awarded the time required to map infall across cores using multiple spectral line observations. To our knowledge, only two previous studies have mapped starless cores in detail to determine infall as a function of position (Williams et al. 1999, 2006). As a result, two fundamental questions are still relatively uncertain: (1) Do core infall speeds have a dependency on the observed position within the core? (2) Do core infall speeds have a dependency on the chosen molecular tracer? To answer these questions, we have obtained IRAM 30m maps of N_2H^+(1-0), DCO^+(2-1), DCO^+(3-2) and HCO^+(3-2) emission towards two prestellar cores (L1544 and L694) and one protostellar (L1521F).

Considering that the process of core collapse is believed to operate from the inside-out with the fastest inward motions toward the center, observations should reveal a radial gradient of infall velocities with diminishing speeds corresponding to farther distances from the core center. Additionally, since core chemistry is affected by the distance from the core center, observations should also reveal the dependency of infall velocity upon the chosen molecular tracer. In chemically evolved cores, molecular tracers found only in the high

density core centers will most likely produce the fastest infall speeds, whereas tracers found only in the low density outer regions will produce slower speeds.

This paper will describe the observations used for our survey in section 2, outline the techniques and models used to analyze the data in section 3, report the characteristics and errors of our results in section 4, discuss possible interpretations and causes of our velocity measurements in section 5, and determine goals of future studies in section 6.

2. Observations

2.1. Targets

The three dense cores of this analysis have been well studied over the past several years. L1544 and L694 have both been classified as prestellar due to the absence of a detectable young stellar object (Ward-Thompson et al. 1994; Harvey et al. 2003). Although L1521F was originally thought to be prestellar, it has recently been found to be protostellar with a confirmed bipolar outflow originating from an embedded VeLLO (Bourke et al. 2006; Takahashi et al. 2013). All three cores have been found to have signatures of infall asymmetries in single pointing surveys (Schnee et al. 2013; Crapsi et al. 2005, etc.). High resolution spectral line emission maps have also been observed toward L1544 (Williams et al. 1999) and L694 (Williams et al. 2006) which have shown a radial gradient of infall speeds across both cores with decreasing speeds as distance from the center increases. However, both of these studies were limited by the fact that they only used a single molecular tracer (N_2H^+(1-0)) which prevents the determination of the dependency of infall upon gas density. Table 1 outlines the physical characteristics of the three targets and includes their velocity measurements from the Schnee et al. (2013) single pointing HCO^+(3-2) survey.

2.2. Molecular Tracers

Rotational emission from molecules is used to observe the kinematics of dense cores. Electrons within these molecules are excited to higher energy levels by collisions or radiation and as they spin down to lower energy levels they emit photons at specific frequencies that can be measured. The four molecules used for our observations were chosen because they trace different densities and therefore allow us to determine infall speeds at multiple depths. The effective critical density (n_{cr}) of HCO^+(3-2), 6.3×10^4 cm^{-3} (Evans II 1999), represents the outer, less dense, core layers. On the other hand, N_2H^+(1-0) and DCO^+(3-2)/(2-1) trace the central, high density regions with each having a n_{cr} around 2×10^5 cm^{-3} (Friesen et al. 2010). Although the DCO^+(3-2) & (2-1) transitions have similar critical densities, they inevitably trace different core layers due to abundance region differences. The (3-2) transition requires slightly higher excitation energies than that of the (2-1). For this reason, it may be that DCO^+(3-2) emission originates from a slightly smaller abundance region, while DCO^+(2-1) traces a broader area defined by a wider range of core depths.

2.3. Data Acquisition

Our observations were obtained at the IRAM 30m single dish telescope in Sierra Nevada, Spain. Frequency windows were centered on N_2H^+(1-0) at 93.174 GHz, DCO^+(2-1) at 144.077 GHz, DCO^+(3-2) at 216.113 GHz, and HCO^+(3-2) at 267.558 GHz. Beam widths were 27", 18", 12" and 10" FWHM for each molecule, respectively. The observed frequencies correspond to a range of emission wavelengths from 3.25 - 1.10 millimeters. Spectral resolutions were within the range of 0.020 - 0.054 km s^{-1} depending on the molecule. See Table 2 for a summary of these observation characteristics. Spectra were obtained at 72 different locations within L694, separated by increments of 10 and 20 arcsec. For L1544, five different locations were observed in a "cross-hairs" orientation with

separations of 20 arcsec. Lastly, a 42 point columnated pattern with equal separations of 20 arcsec was adopted for L1521F. Figure 5 shows the SCUBA 850 μm dust continuum emission overlaid with red circles that represent the points at which spectra were measured in each core.

3. Analysis

3.1. Infall/Outflow Models

Radiative transfer models that reproduce the spectral asymmetries characteristic of collapsing cores have been created so that the infall/outflow velocities of a given core can be extracted from its observed spectra. The two most widely used spectral-line models are the "two-layer" model from Myers et al. (1996) and the more recent "HILL5" model from De Vries & Myers (2005). Although these models are similar, there are slight differences between the two arising from the assumptions they make about core structure. Both assume that there are two regions within a core, but they differ in how the excitation temperature increases between those two layers as a function of opacity. The two-layer model assumes that the excitation temperature increases as a step function at the boundary between the two regions, while the HILL5 model assumes the excitation temperature increases linearly up to a peak at the boundary and then decreases linearly back down to the initial temperature. The equations that represent each model are both composed of five free parameters. For the two-layer, these parameters are (1) the rear excitation temperature (T_r) (excitation temperature of the layer farthest from our point of view), (2) the velocity dispersion of the molecular tracer (σ), (3) the optical depth of the molecular tracer (τ) (the opacity at which the molecule's emission originates), (4) the velocity of the cloud with respect to the local standard of rest (v_{lsr}), and (5) the infall velocity of the system (v_{in}). For the HILL5 model, the only difference is that T_r is replaced by the *peak* excitation

temperature.

3.2.   Line Fitting

After obtaining the reduced data, spectra were fitted using both the two-layer and HILL5 infall models as well as a simple Gaussian model. Two parameters were recorded: (1) the brightness temperature (intensity) of the molecular line emission and (2) the velocity that represents the frequency at which the measurement was made. Using these values as y and x coordinates, respectively, spectral lines were constructed that represent the emission originating from a particular position within each core.

Each model was fitted to the spectra using the MPFIT suite of non-linear least squares curve fitting functions (Markwardt 2009). The equations of each model were programmed into a computer code that called upon MPFIT to perform series of iterations in which it slightly adjusted the free parameters of the given model until the best fit to a particular spectrum was obtained. The fitting process begins using defined starting parameters that were coded into the computer programs. These values were obtained from previous infall speed surveys, such as those conducted by Schnee et al. (2013) and Crapsi et al. (2005), which found velocity dispersions, peak intensities, local standard of rest velocities, and collapse speeds towards the emission peaks of the three cores in this analysis. MPFIT inserts these initial parameters into the equations of the model and compares the theoretically produced line profile with that of the actual data. It then repeats this process, shifting one of the five parameters each time, in attempt to minimize the sum of the squares of the errors between the two lines. Finally, infall/outflow velocities were extracted from the best fits to each of the spectra. These velocities can be seen in Tables 4-6 for each molecular tracer and observed position.

For the purposes of this analysis, it is assumed that the data are accurate and provide a true representation of the emission from each core. Uncertainties in our measurements arise from two main sources: (1) random noise and (2) systematic errors. In addition to noise introduced by the telescope receiver and the various hardware used for its operation, Earth's atmosphere serves as the main source of noise for submillimeter observations. Observing modes have been created in attempts to subtract atmospheric emission from actual signal, but these have limitations. Frequency switching, which involves taking multiple measurements over a range of several MHz by shifting in small increments of Hz, was the mode adopted for this survey. After observations were obtained, estimates for the Earth's atmospheric emission at the observed frequencies was subtracted from each of the measurements. Error is introduced due to the fact that too much, or too little, emission may be subtracted in this process. Without knowing the exact value that the atmosphere emits at each frequency, these errors are unavoidable. However, most random noise will average down to zero if enough integration time on source is used during observations.

The excess noise in a given spectrum can be estimated using the standard deviation of the redshifted and blueshifted sides of the emission peak(s) (i.e. the parts of the spectrum where no clear detections were recorded). In this survey, standard deviations were calculated and used to determine the signal-to-noise ratio (SNR) of each spectrum. In further attempts to reduce inaccuracies in the model fits, this analysis was also conducted using only the spectra that had SNR ≥ 8. Additionally, standard deviations were used as error estimates for MPFIT, which calculates the uncertainty in its final line fit parameters based on user defined error approximations. The MPFIT calculated error estimates for the measured infall/outflow velocities can be seen as $\pm$ values in Tables 4-6.

Uncertainties can also be introduced due to systematic errors when making observations. For instance, the absolute flux calibrator that detects the intensity of the emission we

observe could contain error due to uncertainties in the telescope's efficiency classification and/or the model used for calibration. Essentially, this type of error effects the brightness temperatures (y-axis) of the final spectra by shifting all fluxes either above or below their actual value by the same multiplying factor. Systematic uncertainties can also be introduced by misidentifying the rest frequency of the observed molecular line transition. This type of error effects the observed velocities (x-axis) of a given spectrum by shifting all measurements by the amount that the rest frequency was misclassified. For the type of survey presented in this paper, which involves using the shape of spectra to derive infall/outflow speeds, both flux calibrator and rest frequency uncertainties will fortunately not change the overall results by a significant amount. The infall/outflow models chosen for this analysis use the absorption in the spectra as the criterion for measuring infall velocities. Increasing/decreasing the overall intensities of the spectra and/or shifting their rest frequency would result in little to no alterations in the derived infall speeds since these speeds are not dependent upon those parameters. Therefore, the calculations presented in this paper take into account the random noise in the observed spectra. We do not treat the uncertainties due to systematic errors, but these should be small compared to the uncertainties due to noise.

4. Results

Although the spectra were initially fitted using all three of the aforementioned models, the HILL5 model consistently provided the best fits with the lowest errors. Considering the high volume of double peaked line profiles obtained from this survey, which the Gaussian and two-layer models fail to reproduce, this outcome was predicted. Figure 6 displays the discrepancies between the three models. These results confirm those of De Vries & Myers (2005), which found that the HILL5 model outperformed the two-layer model when fitting

spectra with two peaks. For this reason, the best fits to the HILL5 model were used to obtain the infall/outflow velocity estimates for the final analysis.

Using the HILL5 infall/outflow measurements, velocity gradient maps were constructed which show how fast or slow each core is either collapsing or expanding at each observed position in each molecule. Figures 7-9 show the 12 total maps that were created. Positive velocities (yellow, orange and red) correspond to infall, while negative velocities (green and blue) represent outflow. Due to the fact that spectra with SNR < 8 were removed from the analysis to prevent increased errors in the measurements, there are differences in the mapped coverage across the four molecules. DCO^+(3-2) and HCO^+(3-2) produced the noisiest spectra in our sample, which caused their coverage to be significantly diminished. Due to the high calculated uncertainties in some of our measurements, these velocity maps must be viewed with errors in mind. For this reason, speeds that are below three times their estimated error have been identified and represented by black squares in Figures 10-12. The large uncertainties of DCO^+(3-2) spectra are reflected in the large number of black positions for all three cores in this molecule.

5.   Discussion

5.1.   Radial Dependency

As cloud collapse theory predicted, there are significant velocity variations across all three cores with higher infall speeds generally concentrated toward the center. Measured central minus outer differences were on the order of 100 m s^{-1} for L1521F and L694. Larger radial variations are seen in L694 and L1521F than L1544, but this is more than likely due to the fact that a much smaller region was mapped for the latter. This radial dependency is seen across all four molecules. It can be argued that geometrical orientation effects

undoubtedly play a role in this trend. Since the emission we observe is only the component along our line of sight to each core, we only get a fraction of the full infall/outflow speed vector when making measurements. If the core is taken to be spherical and collapsing, these line of sight effects alone imply decreasing speeds with distance from the center. In that case, the full infall component would be seen at the sphere's absolute center since our line of sight is aligned with the collapse direction at that position, while the slowest speeds would be on the edges where our line of sight is at an approximately 90 degree angle from the collapse direction. However, we have no way of knowing whether the cores we observe are indeed spherical or are collimated with extended structure toward or away from our point of view. For these reasons, we must say that our measured infall/outflow velocities are a lower limit. Depending on the geometry of the core, the full velocity components may potentially be significantly larger.

5.2. Molecular Dependency

The choice of molecular tracer also seems to play an important role for infall measurements, as the ranges of v_{in} magnitudes vary significantly amongst the four molecules. Table 3 shows the averages of the speeds measured by each molecule in each core; calculated using the absolute values of the velocities to account for the negative outflows. On average, DCO^+(2-1) returned the highest infall speeds, followed by N_2H^+(1-0), DCO^+(3-2) and HCO^+(3-2), in both L1544 and L1521F. In L694, HCO^+(3-2) actually produced the fastest inward motions, with DCO^+(2-1) being slightly slower and followed by DCO^+(3-2) and finally N_2H^+(1-0).

These interesting results do not quite match our current understanding of core chemical dynamics. Given the four tracers used in the survey, one would expect N_2H^+(1-0) to produce the fastest inward motions since it traces the higher density central regions where

infall is theorized to be largest based on the inside-out collapse model. On the other hand, HCO^+(3-2), which is thought to be a lower density tracer, would be predicted to yield the slowest speeds since it represents the sparse outer layers where CO can survive in the gas phase and where infall is expected to be weakest. DCO^+ is somewhat of an oddball due to the fact that it contains both deuterium, which traces central regions, and also CO, which traces outer regions. Therefore, one might presume that DCO^+ could trace a middle ground within cores where both deuterium and CO can be produced in the gas phase. The current chemical model also predicts a discrepancy in the measurements for the DCO^+(2-1) and (3-2) transitions due to the fact that the latter occurs at higher densities than the former. More energy is required to excite molecules to higher energy levels. As a result, the abundance region of the (3-2) transition would be smaller because it can only occur deep within the core where densities are higher, more collisions can occur and higher activation energies can be obtained. The (2-1) transition's abundance region would be more extended because it requires less energy and can occur in the low density outer regions as well as the high density inner regions. These differences would cause more pronounced absorption dips in the spectra of DCO^+(2-1), since there is a higher probability that its emission will be reabsorbed, leading to greater calculated infall velocities.

L1544 and L1521F match this chemical model fairly well, with only DCO^+(2-1) being out of place producing the largest infall velocities. It may be that this molecule is actually found deeper into the core than originally believed. CO could be surviving in the gas phase at higher densities and producing DCO^+ within deeper regions of these particular cores, resulting in faster than expected observed infall velocities. The discrepancy between the two transitions (2-1 and 3-2) is possibly arising from the relative sizes of the core layers from which each emission originates. DCO^+(2-1) emission most likely occurs in a much broader region due to the fact that it is a lower energy transition requiring lower energy levels that can be obtained in both high density and lower density regions of the core. As this emission

passes through its wider absorption layer, it may get reabsorbed more frequently causing larger asymmetries in the spectra that we observe. On the other hand, the (3-2) transition is confined to only the regions where particle densities are high enough for the molecule to acquire the excitation energy required to excite it into the higher energy state. This undoubtedly represents a slimmer region of the core, which could lead to lower emission reabsorption rates causing weaker asymmetries and, thus, slower calculated infall speeds.

In L694, we see significantly different behavior. HCO^+ actually produces the largest speeds while N_2H^+ yields the lowest and DCO^+ lies in the middle of the range. One explanation could be that L694 is not as chemically evolved as L1544 and L1521F. Since the abundance regions of particular molecules is relative to evolutionary stage, the tracers used in this survey may not be representing exactly the same areas in each of the cores. From previous studies we know that L1521F is protostellar and thus farther along its life cycle than L1544 and L694. Our observations match this fact since L1521F shows somewhat of a correlation to the chemical expectancies. Our data also suggest that L1544 is farther along the chemical evolution process than L694 since it too displays the theoretical chemistry dynamics. Crapsi et al. (2005) found that L1544 and L694 had similar deuterium fractionation, which is thought to be an indicator of chemical evolution in starless cores, with the former having $[N(N_2D^+)/N(N_2H^+)] = 0.23 \pm 0.04$ and the latter having $[N(N_2D^+)/N(N_2H^+)] = 0.26 \pm 0.05$. It is within the reported errors that L1544 could have a slightly higher fraction than L694 and be a bit farther along the evolution process. It may also be that there are other, less obvious factors impacting the chemical dynamics in L694 that we are presently unaware.

5.3. Outflows

Several outflows were also detected in this analysis along the outer regions of both L1521F and L694. These were to be expected in L1521F considering it has been classified as protostellar and a confirmed bipolar outflow has been detected in previous observations (Takahashi et al. 2013). Our measurements confirm this bipolar outflow, as can be seen most apparently in Figures 9a and 9b, which indicate outflows along the south-east and north-west ends of the core. The outflow measurements of L694 are somewhat surprising since it has been classified as prestellar. Both N_2H^+(1-0) and DCO^+(3-2) indicate outflows along the outskirts of the core (see Figure 8b and 8c) within the range of -0.067 km s^{-1} to -0.020 km s^{-1}. Similar outward motions in prestellar cores have been observed in previous surveys such as Sohn et al. (2007), Schnee et al. (2013) and Lee & Myers (2011). Since L694 is starless, it is doubtful that this is an outflow jet characteristic of protostellar sources. It could be that turbulence flows have somehow caused material in these outer regions to be launched back out toward our point of view while the majority of the core continues to collapse and show inward motions. Cores of this nature are oftentimes classified as oscillatory since they show signs of both collapse and expansion (Lada et al. 2003). However, with distance from the core center the SNR of our spectra decreased significantly. As a result, the line profile fits for the outer region spectra have higher errors. This can be seen in Figures 11b and 11c in which all of the detected outflows have been marked as being below three times their error values. Therefore, these outflow detections may be a reflection of misclassified spectral asymmetries due to the higher noise.

Due to the strong outflows of L1521F which disrupt the normal inward motions of prestellar cores, a model which takes into account protostellar characteristics may provide a better estimate for its infall/outflow speeds. Previous studies such as Kang & Kerton (2012) and Myers et al. (1996) have had success fitting protostellar spectra by adding a central

outflow region to the normal HILL5 and two-layer models which can better reproduce the extended wings characteristic of some line profiles. Since many of our spectra from L1521F display broadened lines, it may be worthwhile to repeat the analysis using one of these customized models in order to see if the results are impacted significantly.

6. Future Work

Although only three cores were analyzed in this paper, our knowledge of the early stages of the star formation process could be improved if infall/outflow maps were created for other regions. Expanding our survey to include additional prestellar sources, such as L1197, Oph D and L492, as well as protostellar sources, such as L429 and L328, will allow us to observe the effects that environment has upon collapse kinematics and chemistry. A larger dataset would also enable further comparison of the properties that were observed in our original three cores. For instance, we would be able to determine whether the outflows found on the outskirts of L694 are commonly seen in many other cores or a unique characteristic that is rare. The turbulence patterns of L1521F could also be compared to those of other protostellar sources in order to characterize the bipolar outflow process.

Observing additional molecular line transitions would also provide a beneficial supplement to this survey. If more molecules were used, the dependency of infall upon the choice of tracer could be refined. Using molecules that trace different densities than the four presented in this paper would provide a better overall picture of prestellar collapse as a function of core depth. Popular high density tracers that could be added include the (3-2) transition of both N_2D^+ and N_2H^+, while low density tracers could include HCN and CS. Using the critical densities of each molecular tracer, data cubes which include infall/outflow as a function of both core position and depth could then be created. This would provide a three-dimensional interpretation of core collapse, from which an improved infall/outflow

model could be developed. Current prestellar core collapse models, such as the HILL5 and two-layer, fail to take into account either the molecular tracer used for the observations or the position on the core where measurements were obtained. A new model that considers these additional parameters may provide more accurate spectral line fitting, allowing for more precise infall/outflow speed measurements in future studies.

7. Summary

Theory predicts that the speed at which starless cores collapse is dependent upon the distance from the core center, while chemical dynamics suggest that collapse is also dependent upon the chosen molecular tracer. To test these theoretical dependencies, we observed multiple positions in three cores (2 starless and 1 protostellar) using four molecular tracers and determined infall/outflow velocities based on the shapes of the obtained spectra. We find that velocity measurements do seem to have a dependency upon both the observed position and molecular tracer. Speeds tend to decrease with distance from the core center, which matches the inside-out starless core collapse model (Shu 1977). Both prestellar cores (L1544 and L694) show overall signs of inward motions, with outflows being detected only on the outer positions in some molecules. The protostellar source (L1521F) also showed inward motions, with the exception of prominant bipolar outflows along one axis. Each molecule also produces significantly different velocity magnitudes, likely as a result of differences in each tracer's critical density and the size of their corresponding absorption layers.

These results suggest that both position and molecular tracer must be taken into consideration when attempting to characterize the overall rate at which a core is collapsing. However, if the goal of the study is to simply determine whether a prestellar core is collapsing or stagnant, a single pointing survey using one molecule will most likely be

sufficient as long as the observed position is somewhere near the center of the core. When working with protostellar sources, this approach does not apply due to the unpredictability of the turbulence caused by bipolar outflows.

8. Acknowledgements

REFERENCES

Aikawa, Y., Ohashi, N., Inutsuka, S.-i., Herbst, E., & Takakuwa, S. 2001, ApJ, 552, 639

Bate, M. R., Tricco, T. S., & Price, D. J. 2014, MNRAS, 437, 77

Bergin, E. A., & Tafalla, M. 2007, ARA&A, 45, 339

Bisschop, S. E., Fraser, H. J., Öberg, K. I., van Dishoeck, E. F., & Schlemmer, S. 2006, A&A, 449, 1297

Bourke, T. L., Myers, P. C., II, N. J. E., et al. 2006, The Astrophysical Journal Letters, 649, L37

Caselli, P., Walmsley, C. M., Tafalla, M., Dore, L., & Myers, P. C. 1999, ApJ, 523, L165

Crapsi, A., Caselli, P., Walmsley, C. M., et al. 2005, ApJ, 619, 379

De Vries, C. H., & Myers, P. C. 2005, ApJ, 620, 800

Di Francesco, J., Evans, II, N. J., Caselli, P., et al. 2007, Protostars and Planets V, 17

Evans II, N. J. 1999, Annual Review of Astronomy and Astrophysics, 37, 311

Francesco, J. D., Johnstone, D., Kirk, H., MacKenzie, T., & Ledwosinska, E. 2008, The Astrophysical Journal Supplement Series, 175, 277

Friesen, R. K., Francesco, J. D., Shimajiri, Y., & Takakuwa, S. 2010, The Astrophysical Journal, 708, 1002

Harvey, D. W. A., Wilner, D. J., Lada, C. J., Myers, P. C., & Alves, J. F. 2003, The Astrophysical Journal, 598, 1112

Kang, S.-J., & Kerton, C. R. 2012, The Astrophysical Journal, 759, 13

Kauffmann, J., Bertoldi, F., Evans, II, N. J., & C2D Collaboration. 2005, Astronomische Nachrichten, 326, 878

Lada, C. J., Bergin, E. A., Alves, J. F., & Huard, T. L. 2003, The Astrophysical Journal, 586, 286

Lee, C. W., & Myers, P. C. 2011, ApJ, 734, 60

Lee, C. W., Myers, P. C., & Plume, R. 2004, ApJS, 153, 523

Lee, C. W., Myers, P. C., & Tafalla, M. 1999, ApJ, 526, 788

—. 2001, ApJS, 136, 703

Markwardt, C. B. 2009, in Astronomical Society of the Pacific Conference Series, Vol. 411, Astronomical Data Analysis Software and Systems XVIII, ed. D. A. Bohlender, D. Durand, & P. Dowler, 251

Myers, P. C., Mardones, D., Tafalla, M., Williams, J. P., & Wilner, D. J. 1996, ApJ, 465, L133

Price, D. J., & Bate, M. R. 2009, MNRAS, 398, 33

Price, D. J., Tricco, T. S., & Bate, M. R. 2012, MNRAS, 423, L45

Schnee, S., Brunetti, N., Di Francesco, J., et al. 2013, ArXiv e-prints, arXiv:1309.4103

Shu, F. H. 1977, ApJ, 214, 488

Sohn, J., Lee, C. W., Park, Y.-S., et al. 2007, ApJ, 664, 928

Tafalla, M., Mardones, D., Myers, P. C., et al. 1998, ApJ, 504, 900

Tafalla, M., Myers, P. C., Caselli, P., Walmsley, C. M., & Comito, C. 2002, ApJ, 569, 815

Takahashi, S., Ohashi, N., & Bourke, T. L. 2013, The Astrophysical Journal, 774, 20

Ward-Thompson, D., Scott, P. F., Hills, R. E., & Andre, P. 1994, MNRAS, 268, 276

Williams, J. P., Lee, C. W., & Myers, P. C. 2006, ApJ, 636, 952

Williams, J. P., Myers, P. C., Wilner, D. J., & di Francesco, J. 1999, ApJ, 513, L61
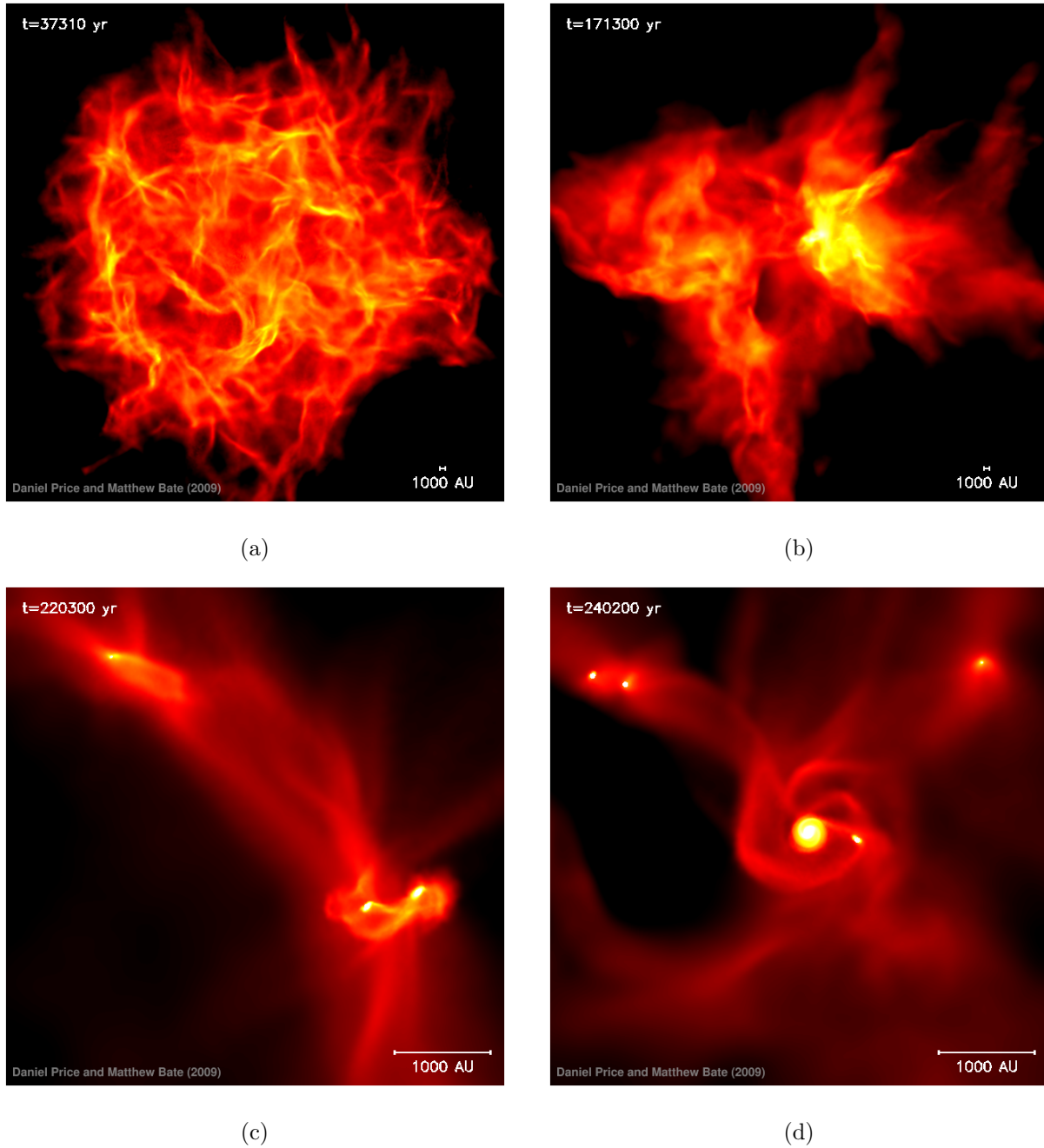
Fig. 1.—: Time-lapse still images from simulations presented in Price & Bate (2009) displaying the collapse of a 50 solar mass molecular cloud to form dense cores. Panels (a) and (b) show the initial contraction of the spherical cloud, which forms higher density clumps represented by yellow. Panels (c) and (d) show the smaller-scale structure within these clumps. As time passes, dense cores of varying sizes begin to coalesce within the densest regions of the cloud.
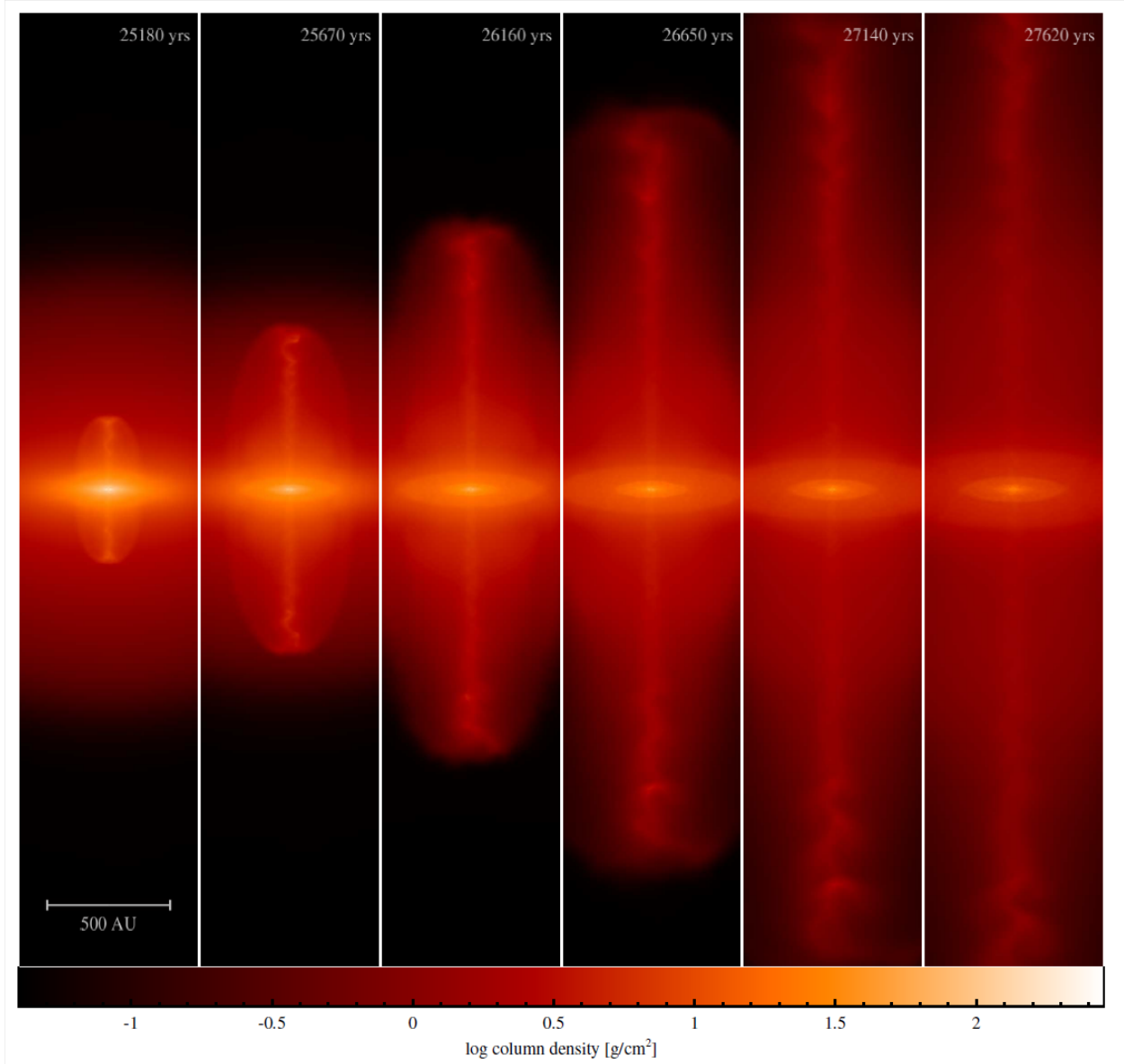
Fig. 2.—: Time-lapse still images from Price et al. (2012) showing the collimated bipolar outflow jets launched by a forming protostar after the collapse of a 1 solar mass dense core. Fuelled by the growing protostar, these jets extend outward along each axis as time passes.
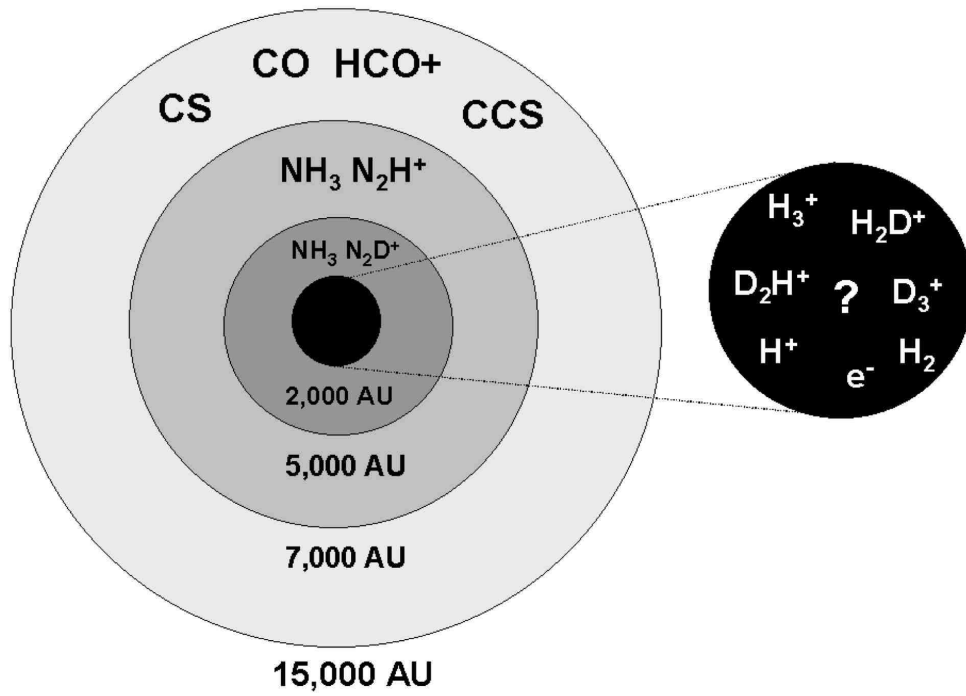
Fig. 3.—: A schematic representation from Di Francesco et al. (2007) of the eventual molecular differentiation within a starless core. The warmer, lower density, outer layers are traced by carbon-bearing molecules. The colder, higher density, inner layers are traced by nitrogen-bearing and deuterated molecules.
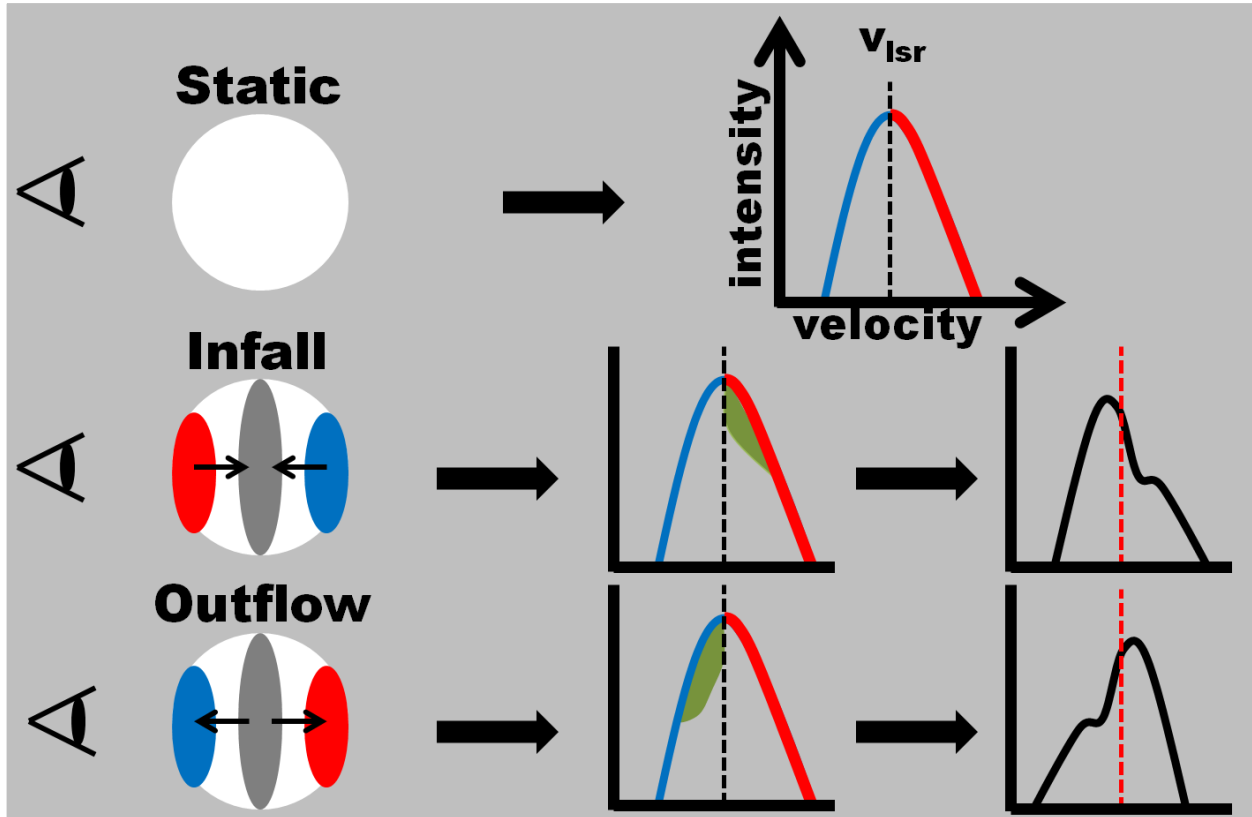
Fig. 4.—: Cartoon displaying the line profile asymmetries that Doppler shifts induce when making core observations. For a given emission line originating from the optically thick central grey region, a static core displays a normal Gaussian distribution, a collapsing core (infall) displays an asymmetrically blue peaked spectrum with respect to the local standard of rest velocity (v_{lsr}) due to absorption in the redshifted velocities, and an expanding core (outflow) displays an asymmetrically red peaked line profile due to absorption in the blueshifted velocities.

(a)

(b)

(c)
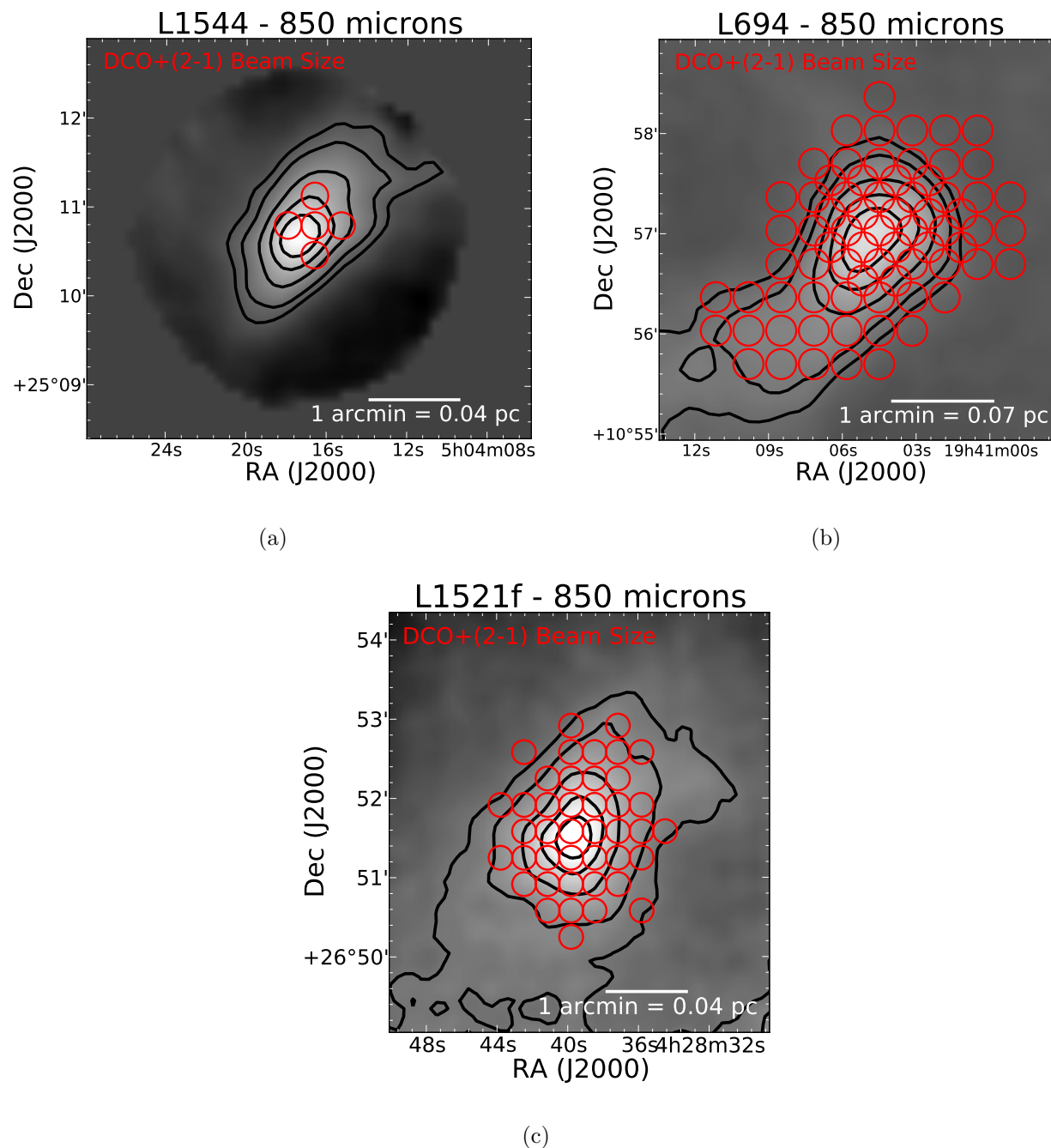
Fig. 5.—: Overview of the observations used in this survey. Background is SCUBA 850 μm dust continuum emission for (a) L1544, (b) L694 and (c) L1521F showing the density structure of each core. Lighter gray corresponds to more emission and therefore higher density. The contours represent 70, 50, 35, 15, and 10 percent of the peak. The red circles correspond to the point at which a spectra was measured and their size represents the DCO$^+$(2-1) beam size.
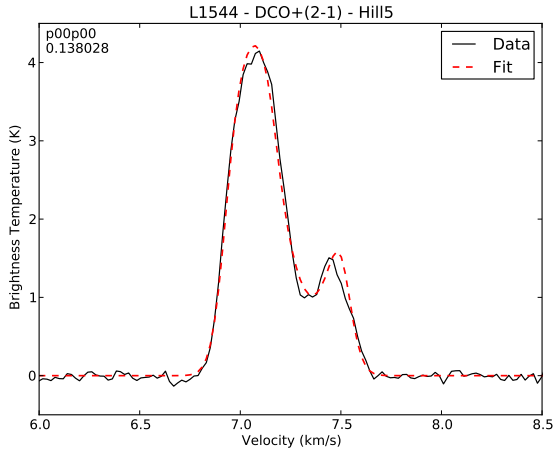
(a)
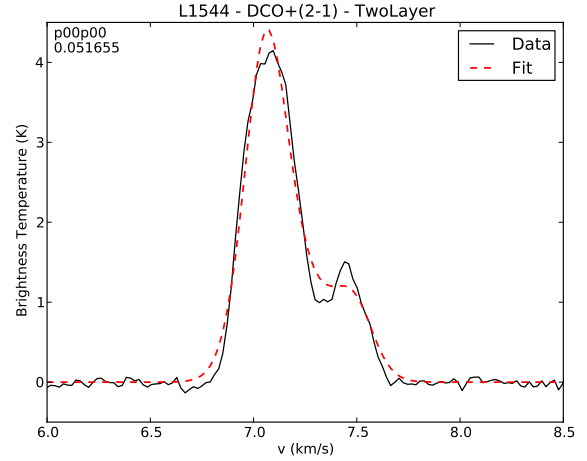
(b)
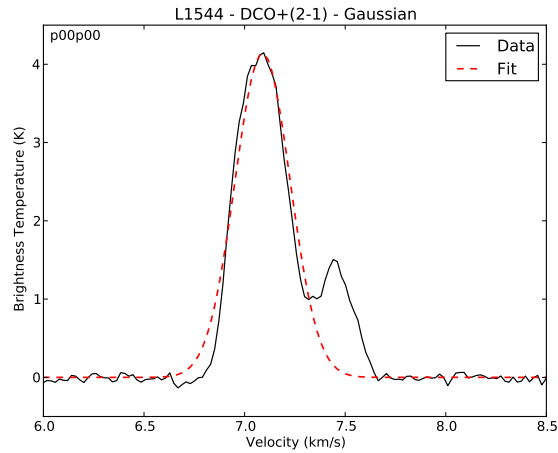
(c)

Fig. 6.—: Example DCO$^+$(2-1) spectrum in L1544 fit with the (a) HILL5, (b) two-layer and (c) Gaussian models. The black line represents the observed DCO$^+$(2-1) spectrum while the red dotted line is the best fit. Notice that the HILL5 model accurately recreates the double peaked line profile while the two-layer and Gaussian fail to sufficiently reproduce the second peak.
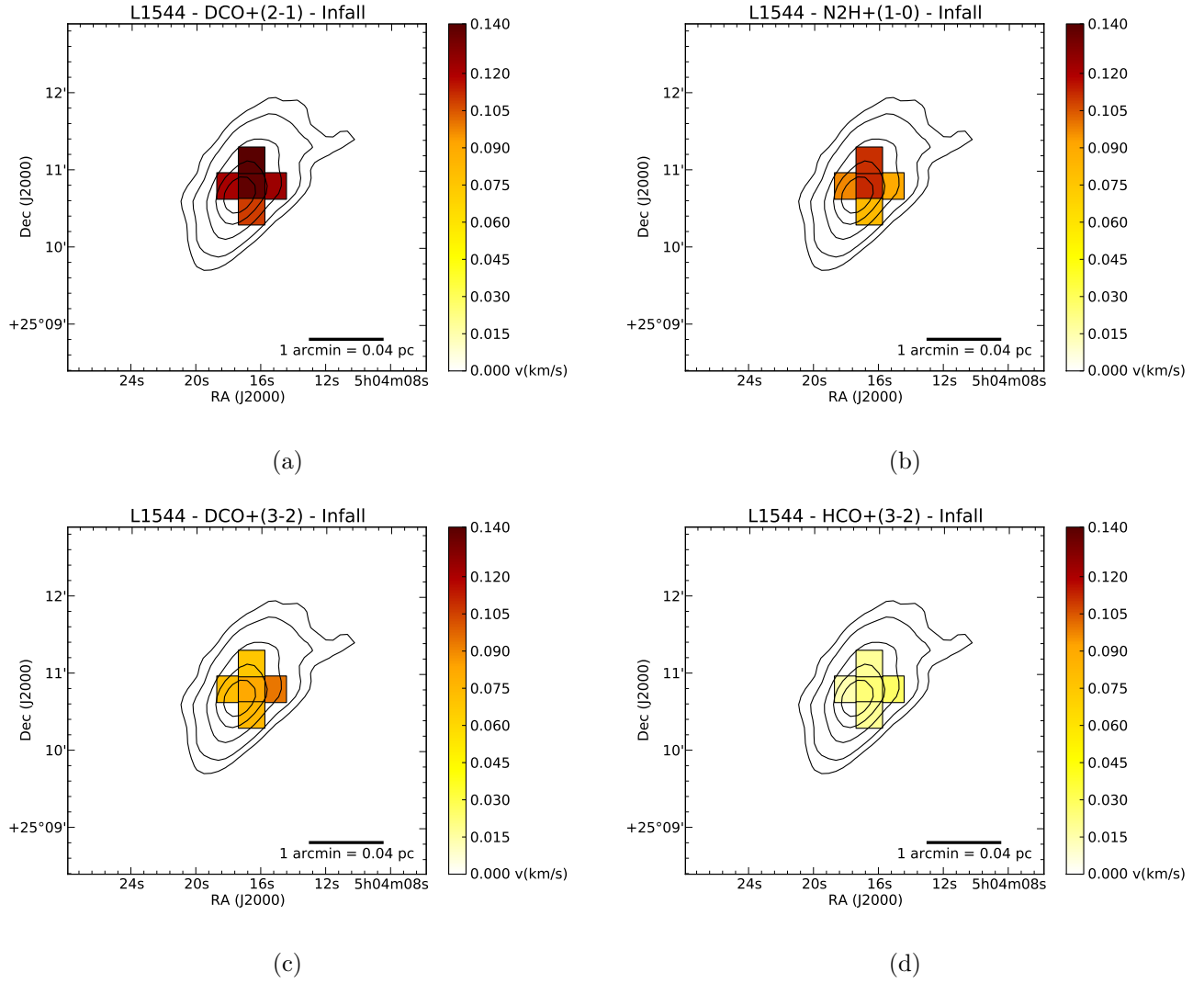
Fig. 7.—: Infall/outflow velocity gradient maps for L1544 in (a) DCO$^+$(2-1) (b) N$_2$H$^+$(1-0) (c) DCO$^+$(3-2) and (d) HCO$^+$(3-2). Velocities are in km s^{-1}. Background contours are the same as in Figure 5a. Note that all four velocity scale bars are uniform.

(a)

(b)

(c)

(d)
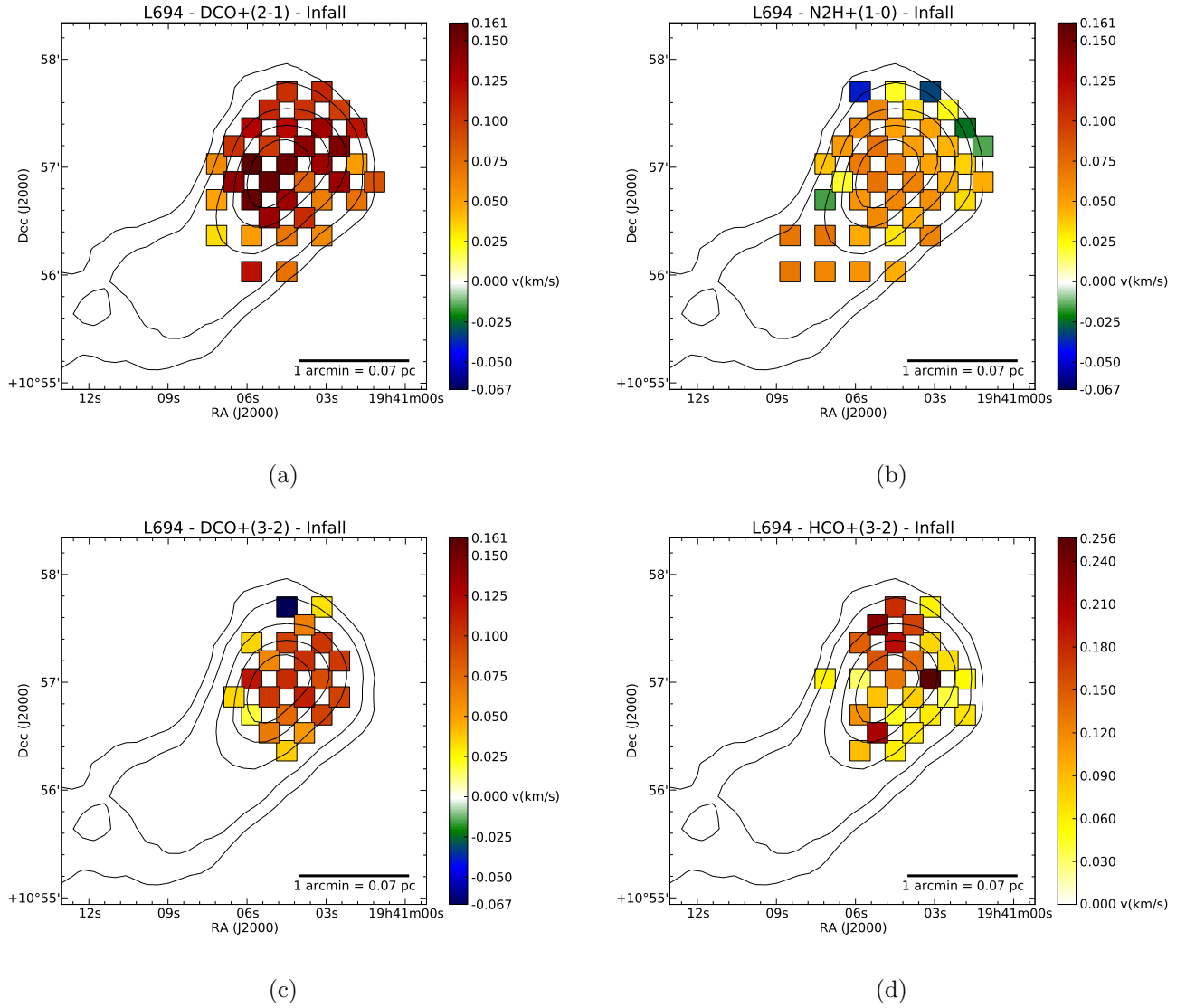
Fig. 8.—: Same as Figure 7, for the core L694. Negative velocities indicate outflow. Note that the velocity scale bar for (d) has been adjusted to accommodate a broader range of infall/outflow speeds.
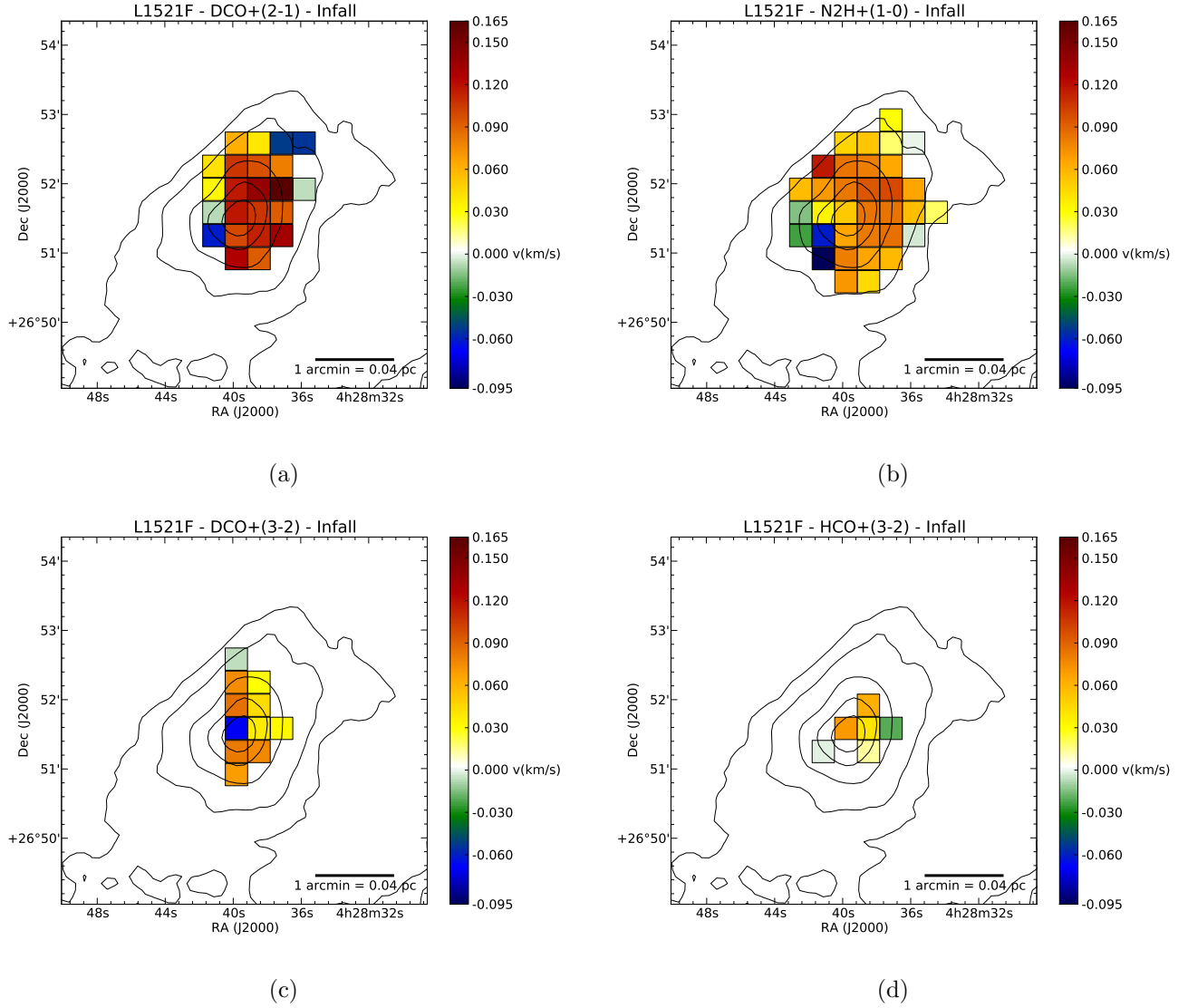
Fig. 9.—: Same as Figure 7, for the core L1521F. Note that all four velocity scale bars are uniform. Outflows can be seen most apparently in the lower left and upper right corners of (a) and (b), which matches the bipolar outflow discovery of Takahashi et al. (2013).
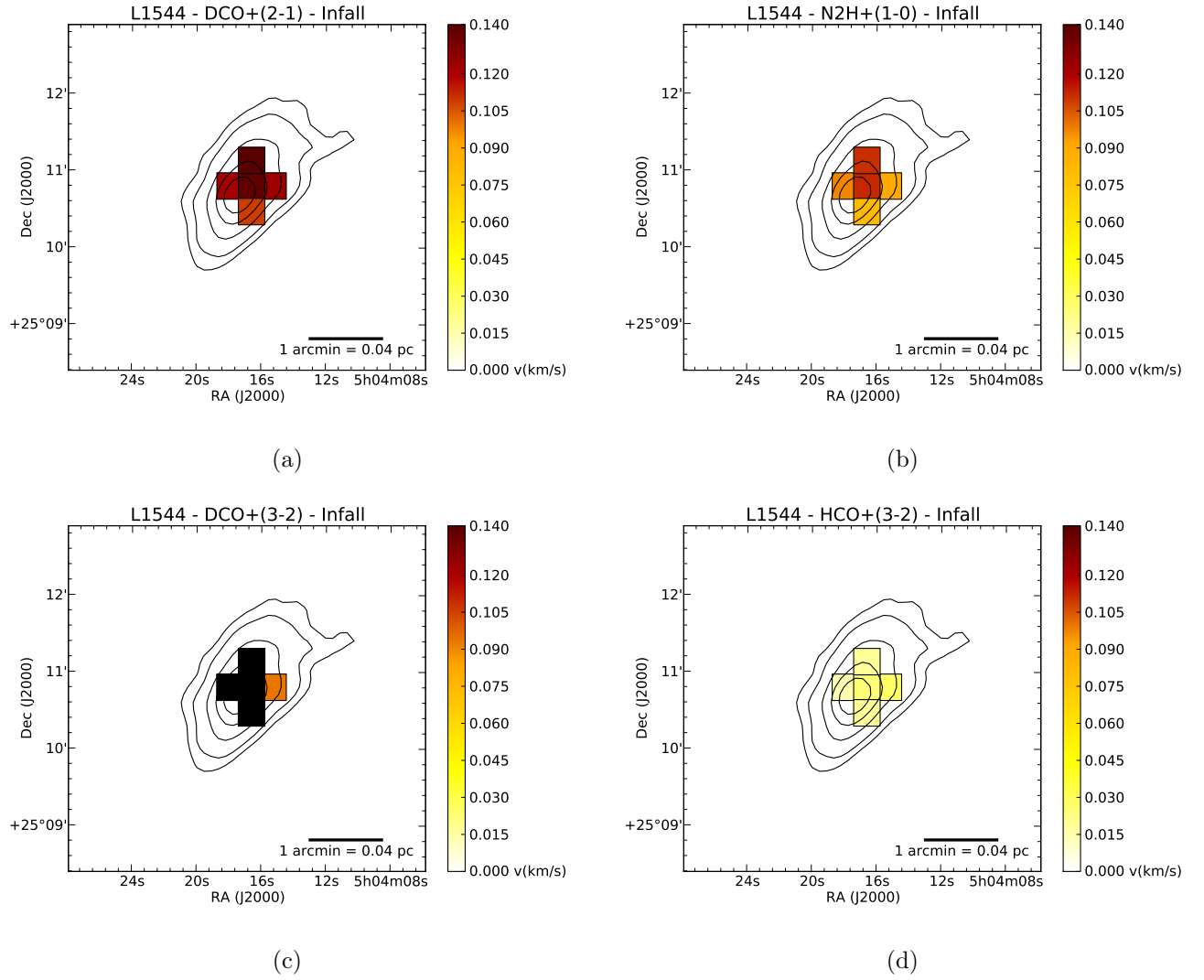
Fig. 10.—: Infall/outflow velocity gradient maps for L1544 with velocities below three times their corresponding error represented by black.

(a)

(b)

(c)

(d)
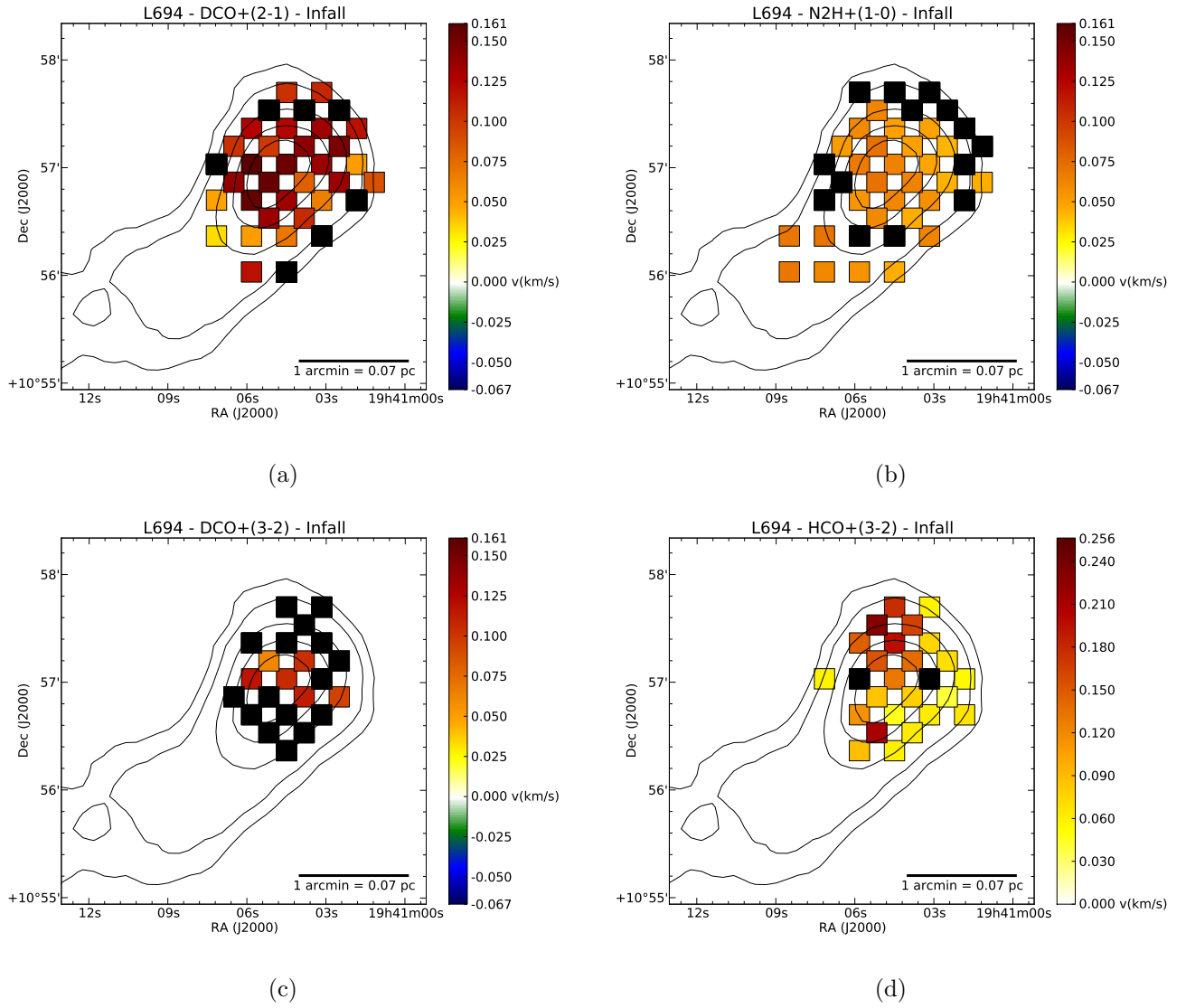
Fig. 11.—: Same as Figure 10, for the core L694
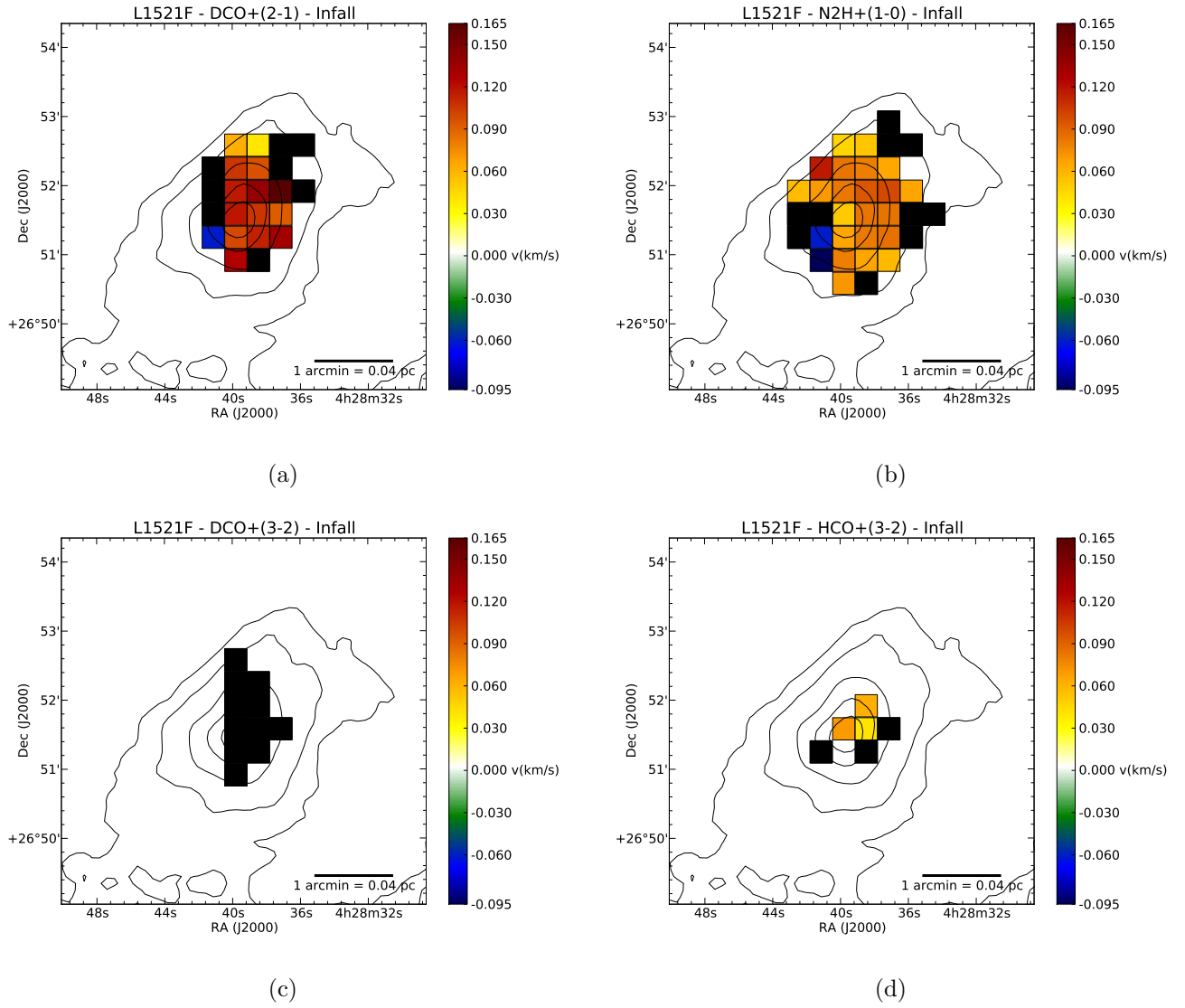
Fig. 12.—: Same as Figure 10, for the core L1521F

Table 1:: Summary of Properties from Literature

Name	Distance[1]	Radius[2]	Radius	Mass[2]	$N(N_2D^+)/N(N_2H^+)$[1]	HCO$^+$(3-2) V_{in} [3]
	pc	"	pc	M_{Sun}		km s^{-1}
L1544	140	60.1	0.041	1.8	0.23 ± 0.04	0.03 ± 0.01
L694	250	66.4	0.080	6.8	0.26 ± 0.05	0.16 ± 0.01
L1521F	140	83.0	0.056	4.4	0.10 ± 0.02	0.42 ± 0.01

[1](Crapsi et al. 2005)

[2](Francesco et al. 2008)

[3](Schnee et al. 2013)

Table 2:: Summary of IRAM Observations

Molecule	Frequency	Wavelength	Angular Resolution	Spectral Resolution
	GHz	mm	"	km s^{-1}
N$_2$H$^+$(1-0)	93.174	3.23	27.0	0.031
DCO$^+$(2-1)	144.077	2.08	17.5	0.020
DCO$^+$(3-2)	216.113	1.39	11.6	0.054
HCO$^+$(3-2)	267.558	1.12	9.41	0.044

Table 3:: Average Velocity Measurements

Core	N$_2$H$^+$(1-0)	DCO$^+$(2-1)	DCO$^+$(3-2)	HCO$^+$(3-2)
	km s^{-1}	km s^{-1}	km s^{-1}	km s^{-1}
L1544	0.098	0.127	0.079	0.021
L694	0.048	0.105	0.076	0.110
L1521f	0.060	0.084	0.055	0.035

Table 4:: L1544 Infall Measurements

No.	RA[1]	Dec[2]	ΔRA[3]	ΔDec[4]	N_2H^+(1-0)[5]	DCO^+(2-1)[6]	DCO^+(3-2)[7]	HCO^+(3-2)[8]
1	05:04:17.93	25:10:48	+20	+00	0.097 ± 0.001	0.122 ± 0.005	0.073 ± 0.055	0.014 ± 0.003
2	05:04:15.27	25:10:48	-20	+00	0.090 ± 0.001	0.124 ± 0.010	0.094 ± 0.009	0.028 ± 0.005
3	05:04:16.60	25:10:48	+00	+00	0.111 ± 0.001	0.138 ± 0.002	0.082 ± 0.029	0.025 ± 0.005
4	05:04:16.60	25:10:28	+00	-20	0.082 ± 0.001	0.109 ± 0.005	0.076 ± 0.081	0.020 ± 0.004
5	05:04:16.60	25:11:08	+00	+20	0.111 ± 0.001	0.140 ± 0.004	0.069 ± 0.085	0.019 ± 0.004

[1]Hours, minutes, seconds (J2000)

[2]Degrees, arcminutes, arcseconds (J2000)

[3]Right Ascension offset in arcsec from central pointing

[3]Declination offset in arcsec from central pointing

[5−8]Measured infall/outflow velocity in km s^{-1} using the specified molecule. Positive indicates infall.

Negative indicates outflow. A blank field indicates the spectra had SNR < 8

Table 5:: L694 Infall Measurements

No.	RA	Dec	ΔRA	ΔDec	N_2H^+(1-0)	DCO^+(2-1)	DCO^+(3-2)	HCO^+(3-2)
1	19:41:04.5	10:57:02	+00	+00	0.064 ± 0.001	0.154 ± 0.001	0.106 ± 0.016	0.202 ± 0.003
2	19:41:01.84	10:58:02	-40	+60				
3	19:41:00.51	10:58:02	-60	+60				
4	19:41:01.84	10:57:42	-40	+40				
5	19:41:00.51	10:57:42	-60	+40				
6	19:41:01.84	10:57:22	-40	+20	-0.024 ± 0.012	0.117 ± 0.004		
7	19:41:00.51	10:57:22	-60	+20				
8	19:40:59.18	10:57:22	-80	+20				
9	19:41:01.84	10:57:02	-40	+00	0.036 ± 0.013	0.051 ± 0.008		0.055 ± 0.010
10	19:41:00.51	10:57:02	-60	+00				
11	19:40:59.18	10:57:02	-80	+00				
12	19:41:01.84	10:56:42	-40	-20	0.034 ± 0.015	0.072 ± 0.045		0.067 ± 0.016
13	19:41:00.51	10:56:42	-60	-20				
14	19:41:01.84	10:56:22	-40	-40				
15	19:41:07.16	10:57:42	+40	+40				
16	19:41:04.5	10:58:22	+00	+80				
17	19:41:05.83	10:58:02	+20	+60				
18	19:41:04.5	10:58:02	+00	+60				
19	19:41:03.17	10:58:02	-20	+60				
20	19:41:05.83	10:57:42	+20	+40	-0.039 ± 0.022			
21	19:41:04.5	10:57:42	+00	+40	0.021 ± 0.020	0.103 ± 0.007	-0.067 ± 0.169	0.177 ± 0.025
22	19:41:03.17	10:57:42	-20	+40	-0.032 ± 0.018	0.108 ± 0.012	0.031 ± 0.075	0.057 ± 0.018
23	19:41:05.83	10:57:22	+20	+20	0.060 ± 0.007	0.125 ± 0.010	0.035 ± 0.025	0.146 ± 0.016
24	19:41:04.5	10:57:22	+00	+20	0.049 ± 0.002	0.124 ± 0.019	0.096 ± 0.047	0.095 ± 0.019
25	19:41:03.17	10:57:22	-20	+20	0.048 ± 0.006	0.134 ± 0.010	0.101 ± 0.092	0.075 ± 0.013
26	19:41:05.83	10:57:02	+20	+00	0.067 ± 0.001	0.161 ± 0.002	0.117 ± 0.010	0.032 ± 0.015
27	19:41:03.17	10:57:02	-20	+00	0.048 ± 0.003	0.134 ± 0.002	0.090 ± 0.031	0.029 ± 0.014
28	19:41:05.83	10:56:42	+20	-20	0.055 ± 0.005	0.155 ± 0.003	0.019 ± 0.011	0.115 ± 0.013
29	19:41:04.5	10:56:42	+00	-20	0.061 ± 0.001	0.134 ± 0.003	0.076 ± 0.070	0.045 ± 0.014
30	19:41:03.17	10:56:42	-20	-20	0.057 ± 0.005	0.065 ± 0.008	0.095 ± 0.051	0.062 ± 0.014
31	19:41:05.83	10:56:22	+20	-40	0.046 ± 0.017	0.051 ± 0.007		0.089 ± 0.016
32	19:41:04.5	10:56:22	+00	-40	0.031 ± 0.012	0.069 ± 0.006	0.036 ± 0.028	0.061 ± 0.010
33	19:41:03.17	10:56:22	-20	-40	0.062 ± 0.006	0.060 ± 0.108		

(Same format as Table 4) *Continued on next page*

Table 5 – *Continued from previous page*

No.	RA	Dec	ΔRA	ΔDec	N$_2$H$^+$(1-0)	DCO$^+$(2-1)	DCO$^+$(3-2)	HCO$^+$(3-2)
34	19:41:05.83	10:56:02	+20	-60	0.056 ± 0.007	0.119 ± 0.004		
35	19:41:04.5	10:56:02	+00	-60	0.044 ± 0.012	0.071 ± 0.109		
36	19:41:03.17	10:56:02	-20	-60				
37	19:41:05.83	10:55:42	+20	-80				
38	19:41:04.5	10:55:42	+00	-80				
39	19:41:08.49	10:57:22	+60	+20				
40	19:41:07.16	10:57:22	+40	+20				
41	19:41:08.49	10:57:02	+60	+00				
42	19:41:07.16	10:57:02	+40	+00	0.039 ± 0.023	0.060 ± 0.021		0.059 ± 0.019
43	19:40:59.18	10:56:42	+80	-20				
44	19:41:08.49	10:56:42	+60	-20				
45	19:41:07.16	10:56:42	+40	-20	-0.015 ± 0.025	0.048 ± 0.007		
46	19:41:09.82	10:56:22	+80	-40				
47	19:41:08.49	10:56:22	+60	-40	0.069 ± 0.005			
48	19:41:07.16	10:56:22	+40	-40	0.071 ± 0.004	0.033 ± 0.009		
49	19:41:09.82	10:56:02	+80	-60				
50	19:41:08.49	10:56:02	+60	-60	0.069 ± 0.004			
51	19:41:07.16	10:56:02	+40	-60	0.061 ± 0.008			
52	19:41:09.82	10:55:42	+80	-80				
53	19:41:08.49	10:55:42	+60	-80				
54	19:41:07.16	10:55:42	+40	-80				
55	19:41:06.5	10:57:32	+30	+30				
56	19:41:06.5	10:57:12	+30	+10	0.052 ± 0.016	0.103 ± 0.012		
57	19:41:06.5	10:56:52	+30	-10	0.020 ± 0.014	0.138 ± 0.003	0.034 ± 0.019	
58	19:41:05.17	10:57:32	+10	+30	0.063 ± 0.005	0.109 ± 0.049		0.230 ± 0.010
59	19:41:05.17	10:57:12	+10	+10	0.072 ± 0.002	0.099 ± 0.007	0.062 ± 0.019	0.153 ± 0.023
60	19:41:05.17	10:56:52	+10	-10	0.071 ± 0.002	0.155 ± 0.003	0.100 ± 0.080	0.085 ± 0.019
61	19:41:05.17	10:56:32	+10	-30	0.060 ± 0.003	0.135 ± 0.004	0.068 ± 0.067	0.210 ± 0.008
62	19:41:03.83	10:57:32	-10	+30	0.033 ± 0.012	0.103 ± 0.051	0.066 ± 0.058	0.164 ± 0.010
63	19:41:03.83	10:57:12	-10	+10	0.049 ± 0.004	0.141 ± 0.005	0.104 ± 0.027	0.139 ± 0.014
64	19:41:03.83	10:56:52	-10	-10	0.063 ± 0.003	0.081 ± 0.005	0.112 ± 0.020	0.079 ± 0.013
65	19:41:03.83	10:56:32	-10	-30	0.045 ± 0.006	0.107 ± 0.010	0.052 ± 0.178	0.063 ± 0.014
66	19:41:02.5	10:57:32	-30	+30	0.022 ± 0.015	0.097 ± 0.086		

(Same format as Table 4) *Continued on next page*

Table 5 – *Continued from previous page*

No.	RA	Dec	ΔRA	ΔDec	N_2H^+(1-0)	DCO^+(2-1)	DCO^+(3-2)	HCO^+(3-2)
67	19:41:02.5	10:57:12	-30	+10	0.043 ± 0.008	0.147 ± 0.004	0.099 ± 0.096	0.069 ± 0.015
68	19:41:02.5	10:56:52	-30	-10	0.044 ± 0.007	0.135 ± 0.003	0.095 ± 0.005	0.040 ± 0.012
69	19:41:01.17	10:57:12	-50	+10	-0.015 ± 0.014			
70	19:41:01.17	10:56:52	-50	-10	0.044 ± 0.006	0.087 ± 0.006		
71	19:41:11.15	10:56:22	+100	-40				
72	19:41:11.15	10:56:02	+100	-60				

Table 6:: L1521F Infall Measurements

No.	RA	Dec	ΔRA	ΔDec	N_2H^+(1-0)	DCO^+(2-1)	DCO^+(3-2)	HCO^+(3-2)
1	04:28:39.8	26:51:15	+00	+00	0.066 ± 0.002	0.099 ± 0.005	0.081 ± 0.110	
2	04:28:41.13	26:51:15	+20	+00	-0.061 ± 0.003	-0.061 ± 0.017		-0.001 ± 0.010
3	04:28:42.46	26:51:15	+40	+00	-0.023 ± 0.013			
4	04:28:43.79	26:51:15	+60	+00				
5	04:28:38.47	26:51:15	-20	+00	0.081 ± 0.001	0.114 ± 0.011	0.076 ± 0.171	0.013 ± 0.008
6	04:28:37.14	26:51:15	-40	+00	0.085 ± 0.003	0.132 ± 0.012		
7	04:28:35.81	26:51:15	-60	+00	-0.003 ± 0.214			
8	04:28:42.46	26:50:55	+40	-20				
9	04:28:41.13	26:50:55	+20	-20	-0.095 ± 0.004			
10	04:28:39.8	26:50:55	+00	-20	0.080 ± 0.003	0.126 ± 0.014	0.069 ± 0.302	
11	04:28:38.47	26:50:55	-20	-20	0.066 ± 0.003	0.093 ± 0.084		
12	04:28:37.14	26:50:55	-40	-20	0.057 ± 0.012			
13	04:28:41.13	26:50:35	+20	-40	±			
14	04:28:39.8	26:50:35	+00	-40	0.071 ± 0.004			
15	04:28:38.47	26:50:35	-20	-40	0.045 ± 0.016			
16	04:28:35.81	26:50:35	-60	-40				
17	04:28:39.8	26:50:15	+00	-60				
18	04:28:42.46	26:51:35	+40	+20	-0.014 ± 0.019			
19	04:28:41.13	26:51:35	+20	+20	0.035 ± 0.013	-0.008 ± 0.014		
20	04:28:39.8	26:51:35	+00	+20	0.051 ± 0.002	0.117 ± 0.033	-0.070 ± 0.162	0.070 ± 0.006
21	04:28:38.47	26:51:35	-20	+20	0.083 ± 0.001	0.107 ± 0.002	0.038 ± 0.148	0.041 ± 0.006
22	04:28:37.14	26:51:35	-40	+20	0.085 ± 0.002	0.093 ± 0.031	0.033 ± 0.852	-0.020 ± 0.009
23	04:28:35.81	26:51:35	-60	+20	0.056 ± 0.021			
24	04:28:34.48	26:51:35	-80	+20	0.020 ± 0.523			
25	04:28:43.79	26:51:55	+60	+40				
26	04:28:42.46	26:51:55	+40	+40	0.057 ± 0.010			
27	04:28:41.13	26:51:55	+20	+40	0.070 ± 0.004	0.032 ± 1.235		
28	04:28:39.8	26:51:55	+00	+40	0.083 ± 0.003	0.117 ± 0.020	0.085 ± 0.239	
29	04:28:38.47	26:51:55	-20	+40	0.095 ± 0.001	0.138 ± 0.004	0.044 ± 0.137	0.062 ± 0.008
30	04:28:37.14	26:51:55	-40	+40	0.099 ± 0.003	0.165 ± 0.008		
31	04:28:35.81	26:51:55	-60	+40	0.066 ± 0.003	-0.007 ± 0.022		
32	04:28:41.13	26:52:15	+20	+60	0.117 ± 0.003	0.042 ± 0.030		
33	04:28:39.8	26:52:15	+00	+60	0.083 ± 0.003	0.106 ± 0.018	0.076 ± 0.110	

(Same format as Table 4) *Continued on next page*

Table 6 – *Continued from previous page*

No.	RA	Dec	ΔRA	ΔDec	N_2H^+(1-0)	DCO^+(2-1)	DCO^+(3-2)	HCO^+(3-2)
34	04:28:38.47	26:52:15	-20	+60	0.080 ± 0.003	0.097 ± 0.021	0.029 ± 0.045	
35	04:28:37.14	26:52:15	-40	+60	0.065 ± 0.004	0.080 ± 0.028		
36	04:28:42.46	26:52:35	+40	+80				
37	04:28:39.8	26:52:35	+00	+80	0.047 ± 0.009	0.062 ± 0.019	-0.006 ± 0.019	
38	04:28:38.47	26:52:35	-20	+80	0.053 ± 0.006	0.040 ± 0.008		
39	04:28:37.14	26:52:35	-40	+80	0.019 ± 0.006	-0.052 ± 0.023		
40	04:28:39.8	26:52:55	+00	+100				
41	04:28:37.14	26:52:55	-40	+100	0.029 ± 0.054			
42	04:28:35.81	26:52:35	-60	+80	0.001 ± 0.010	-0.054 ± 0.025		